ORIGINAL ARTICLE

lajss.org© Latin American Journal of Solids and Structures

www.lajss.org

Formation of explosively-formed projectile with tail fins using polygonal charges

Peng Chen[a], Wenbin Li[a*], Yiming Li[a], Dacheng Gao[a]

[a]Ministerial Key Laboratory of ZNDY, Nanjing University of Science and Technology, Nanjing, Jiangsu, China. Email: cp1212@njust.edu.cn, lwb2000cn@njust.edu.cn, Liyiming0919@163.com, gaodacheng001@163.com

* Corresponding author

https://doi.org/10.1590/1679-78257928

Abstract

To further improve the strike accuracy and penetration power of explosively-formed projectile (EFP) after long-distance flight, a polygonal charge capable of forming EFP with tail fins was designed during the study. A model for calculating the EFP velocity was derived from the effective charge and detonation projection theories with the integration of calculus. The circumferential velocity distributions of EFP formed using polygonal charges were obtained using this model, and the mechanisms underlying the formation of tail fins were elucidated. The feasibility of using this polygonal charge to form tail fin EFP was verified by conducting multi-media soft recovery tests and numerical simulations. Furthermore, the feasibility of forming tail fin EFP using polygonal charges with different numbers of sides and the effects of the structural parameters of a hexagonal charge on the formation of tail fin EFP were investigated by simulation. The ranges of optimal values for the structural parameters of a hexagonal charge capable of forming high-performance tail fin EFPs were determined.

Keywords

explosively-formed projectile, tail fin, polygonal charge, numerical simulation

Graphical Abstract

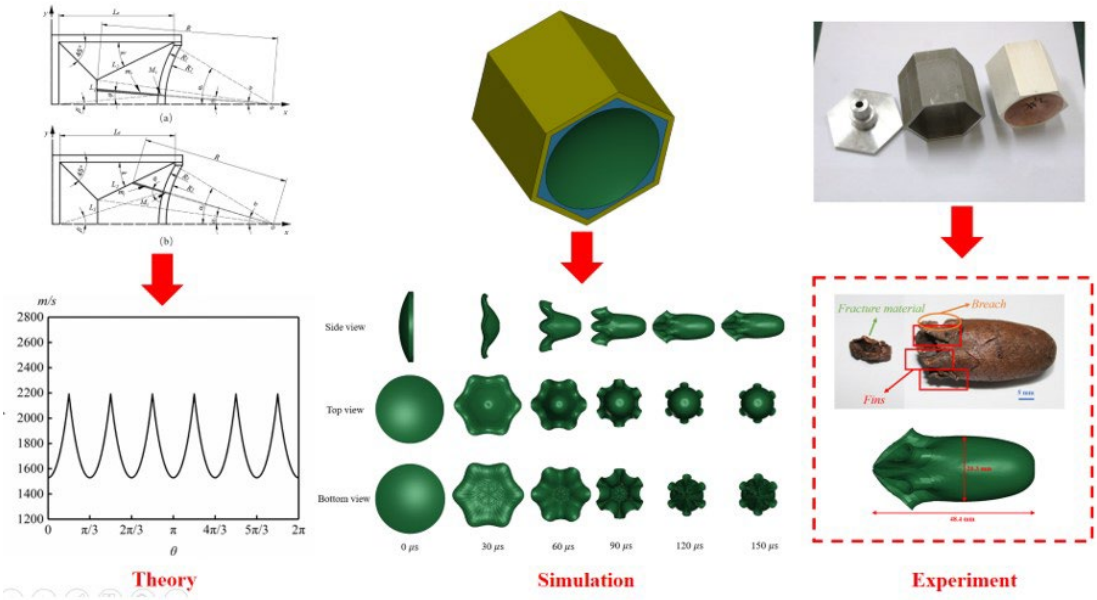

Received: November 14, 2023. In revised form: November 14, 2023. Accepted: November 16, 2023. Available online: November 21, 2023
https://doi.org/10.1590/1679-78257928

Latin American Journal of Solids and Structures. ISSN 1679-7825. Copyright © 2023. This is an Open Access article distributed under the terms of the Creative Commons Attribution License, which permits unrestricted use, distribution, and reproduction in any medium, provided the original work is properly cited.

1 INTRODUCTION

Explosively-formed projectiles (EFPs) have important military applications because they have good penetration performance and are insensitive to the blast height (Chuan Y et al. 1999, Ma et al. 2020). Based on the length-diameter ratio and shape of the projectile, EFP can be classified into spherical EFP and rod-like EFP. Although the spherical EFP can maintain flight stability, its penetration power is relatively low (Wang et al. 2011). One of the fundamental ways of improving the penetration depths of EFP at large standoff distances is to increase their length-to-diameter ratios. However, increasing the length-to-diameter ratio excessively decreases the rod-like EFP flight stability and target accuracy. This challenge presents significant limitations to the development and improvement of shaped charge warhead technology.

To enhance the flight stability and target accuracy of rod-like EFP, researchers have proposed the concept of tail-skirt EFP (Li et al. 2016b). Although the tail-skirt EFP can meet the requirements of flight stability (Wu et al. 2007), the empty tail-skirt structure not only increases flight resistance (Zhu 2014), but also lacks penetration ability. Therefore, it is necessary to replace the tail-skirt structure with a tail wing structure. The inclusion of a regular tail fin at the tail of the EFP can effectively enhance the aerodynamic shape of the rod EFP, leading to improved flight stability and strike accuracy (Liu et al. 2014a, Berner and Flec 1999). Currently, both domestic and international scholars have conducted extensive research on tail EFP formation methods. These studies primarily focus on altering the warhead's detonation mode (Bouet et al. 1995, Li et al. 2007, Liu et al. 2014b, Li et al. 2018), placing waveform regulators (Weimann 1993), employing clapboards (Zhao et al. 2006, Lin et al. 2009, Lin et al. 2013), utilizing stepped liners (Huang and Zhang 2009, Wang et al. 2022), and employing polygonal structures (Men et al. 2002, Weimann 1991). While there are various approaches to investigate the formation of tail fin EFP, they face significant challenges in practical applications. These challenges include the need for precise synchronization in multi-point initiation, the high precision required for waveform regulators or clapboards, as well as the complex design and processing difficulties associated with stepped shaped charge liners. In comparison, utilizing a polygonal structure offers a simpler and more effective method for forming tail fin EFP. As a result, research on employing polygonal structures for tail fin EFP formation has gained considerable attention recently.

To date, researchers have conducted extensive studies on the formation and optimal design of polygonal shells or liners on the tail fin of EFP, and have made significant progress. Tang et al. (2009) investigated the influence of shells with different variable wall thicknesses on the formation of EFP with tail fins. They concluded that different shell shapes can generate corresponding tails and obtained the effects of various wall thicknesses on tail formation through simulations. Yu et al. (2017) through numerical simulations, found that excessively thick polygon shells are not conducive to the development of projectile shape. They determined that when the side length of the steel polygon shell is 0.6-0.65 times the charge diameter, the formation of EFP with tail fins is optimal. Li et al. (2023) conducted numerical simulations on EFP formed by polygonal shells, identified the influence of charge parameters on tail fin EFP performance, and optimized the performance of tail fin EFP using the orthogonal design method. Shi et al. (2010) obtained EFP with inclined fins through numerical simulations of asymmetric stepped shells. Building upon this research, Peng et al. (2022) theoretically analyzed the formation mechanism of tail fin EFP using stepped shell-shaped charges and verified its feasibility through soft recovery tests. Luo et al. (2009) improved the flight performance of tail fin EFP by modifying the liner edge with concave dents and optimizing the warhead structural parameters using numerical simulations. Zhang et al. (2004) and Li et al. (2019) proposed polygonal liners and used numerical simulations to obtain tail fin EFP with large length-to-diameter ratios. The symmetry of the molded fins plays a crucial role in ensuring the flight stability of the EFP. (Li et al. 2016a) Compared with the polygonal shell or the liner, the use of polygonal charge can avoid the influence of asymmetry caused by machining errors. Furthermore, there are limited reports on the formation mechanism analysis and experimental research of tail fin EFP under polygonal charge.

In this study, a polygonal charge EFP warhead that can form a tail fin EFP is proposed. The circumferential velocity distributions of EFP formed using polygonal charges were obtained using theoretical calculation, and the mechanisms underlying the formation of tail fins were elucidated. The feasibility of using polygonal charges to form tail fin EFP and the reliability of using numerical simulations were verified by comparing tail fin EFP recovered from multi-media soft recovery tests with the simulation results,and the deformation and velocity distribution of the liner under hexagonal charge are analyzed. Finally, with consistent simulation and experimental results, the characteristics of tail fin EFP formed using polygonal charges were investigated. The results provide data and technical support for tail fin EFP formation.

2 MECHANISMS UNDERLYING TAIL FIN EFP FORMATION

2.1 Crushing velocity of liner element

During the explosion, the detonation products fly in different directions, and only the detonation products produced by a portion of the charge fly in the preset direction necessary to project the liner. This portion of the charge is referred to as the effective charge (Orilenko 2011). Figure 1 illustrates the effective charge of EFP warhead with a shell. For the endpoint detonation charge, it is necessary to consider the end effect, which involves creating a cone-shaped cavity at the detonation end. The cone height is equal to the charge radius. As a result, the angle formed between the side line of the cone and the side line of the charge is 45° (Wang and Zhao 1993). When the charge height satisfies $L \geq 1.5D_c$, the effective charge is approximately a cone with a base radius equal to $D_c/2$ and a height equal to $l_a = D_c$. For an EFP without a shell, when the charge is short ($L < 1.5D_c$), the effective charge is approximately a circular truncated cone with a taper angle of 53.2°. The angle between the sides of the charge and the effective charge, k, can be calculated from l_a and r (Kennedy 1998):

$$k = \arctan(l_a / 2D_c) = \arctan(1/2) \approx 26.6^{\circ} \tag{1}$$

For an EFP shaped charge with a shell, k can be calculated from the masses of the shell and the charge, M and m, using the modified model presented in Equation (6) (Benham 1979):

$$k = \frac{26.6^{\circ}}{\sqrt{2\frac{M}{m}+1}} \tag{2}$$

where ρ_s and ρ_c are the densities of the charge and the shell, respectively.

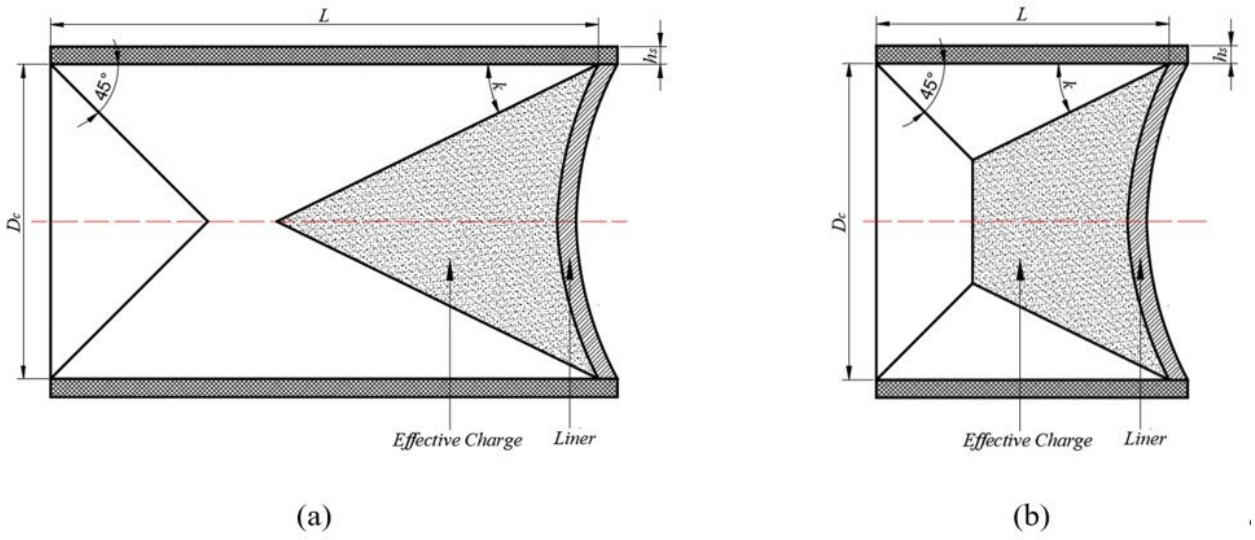

Figure 1 The effective charge. (a) $L \geq 1.5D_c$.(b) $L < 1.5D_c$.

By assuming that the motion of each infinitesimal liner element is produced by the one-dimensional projection from the explosive and that the effects of the lateral rarefaction wave and the interactions between the infinitesimal elements are negligible, Equation (3) was obtained (Orilenko 2011):

$$M\frac{dV}{dt} = SP \tag{3}$$

In Equation (3), M and S represent the mass and area of each infinitesimal element, respectively.

When the explosion products of the explosive column fly in the direction perpendicular to the metal surface and the resulting projection of the metal is assumed to be one-dimensional, the relationship between the pressure acting on the surface of the rigid wall, P, and the time, t, can be expressed by Equation (4):

$$P = \frac{64}{27} P_H (\frac{L}{Dt})^3 \tag{4}$$

where P_H represents the wave front pressure, L is the charge height, and D is the detonation velocity of the explosive.

However, given that the metal is not a rigid body, the pressure on the surface of the projected body is lower than that given by Equation (4). Hence, Equation (4) was modified to express the temporal variations in the pressure produced by the detonation products on the non-rigid metal body (Cao 1998):

$$P = 1.68 P_H (\frac{L}{Dt})^3 \tag{5}$$

Since the liner is concave, the detonation wave impacts each infinitesimal element at an oblique angle. The pressure produced by the detonation wave on the surface of the rigid wall varies with the incident angle of the detonation wave, φ, and time. It can be expressed by Equation (6) (Cao 1998):

$$P = (0.68 + \cos\varphi) P_H (\frac{L}{Dt})^3 \tag{6}$$

By substituting Equations (6) into Equation (3) and integrating, an expression for the crushing velocities of the infinitesimal flat plate and liner elements could be obtained:

$$v_i = \frac{1}{8}(0.68 + \cos\varphi)\frac{m_i}{M_i} D \tag{7}$$

In Equation (7), φ represents the angle between the detonation wave front and the plane tangent to the infinitesimal liner element, m_i is the mass of the effective charge corresponding to the infinitesimal liner element, and M_i is the mass of the infinitesimal liner element.

2.2 Structure of the polygonal EFP shaped charge

EFP charges with different polygonal shapes (polygons with different numbers of sides) can be created. The EFP charge used in this study had a sub-caliber structure consisting of a polygonal main charge, a hemispherical liner, and a polygonal shell. The charge diameter, D_c, and the shell thickness, hs, varied periodically with inscribed angle, ϑ. The other geometric parameters of the charge did not vary in the circumferential direction. Figure 2 depicts geometric models for three different polygonal (hexagonal, octagonal, and decagonal) EFP shaped charges with equal minimum shell thickness, h_{s0}, and subcaliber thicknesses, t_0.

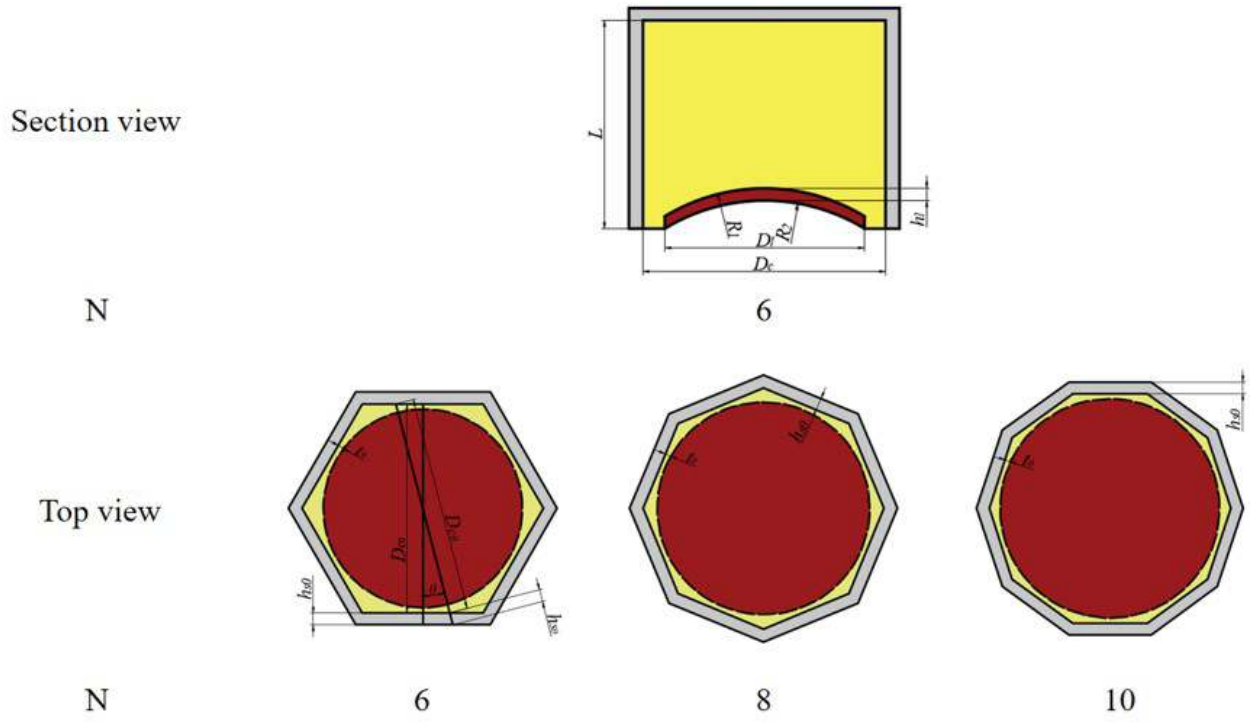

Figure 2 Geometric models for three different polygonal charges.

During the first charge interval ($0 \le \vartheta \le 2\pi/N$, where N, which is a positive integer larger than 2, is the number of polygon sides), shown in Figure 2, the charge radius, $D_{c\vartheta}$, and the shell thickness, hs_ϑ, first increase and then decrease as ϑ increases. They reach their minimum values, designated as D_{c0} and h_{s0}, respectively, when $\vartheta = 0$ and $2\pi/N$:

$$D_{c\theta} = D_{c0} / \cos\theta \tag{8}$$

$$hs_\theta = hs_0 / \cos\theta \tag{9}$$

Figure 3 shows the geometric model of a typical polygonal shell for N = 6. At the moment of explosion, the motion of each infinitesimal element of the shell is independent of the other infinitesimal elements in the circumferential direction. This is also true for the motion of the explosion products and the liner. Thus, the masses of the shell and the charge within each infinitesimal angle, $d\vartheta$, can be calculated according to Equations (10) and (11):

$$M_s = \rho_s L \cdot dS_\theta = \rho_s L r_{c\theta} h_{s\theta} \cdot d\theta \tag{10}$$

$$m_c = \frac{1}{2}\rho_c L r_{c\theta}^2 \cdot d\theta \tag{11}$$

where $d\vartheta$ represents the infinitesimal angle in the axial cross-section of the charge, ρ_s and ρ_c are the densities of the shell and charge, respectively, L is the charge height, dS_ϑ is the area of the infinitesimal element of the shell in the axial cross-section, and M_s and m_c represent the masses of the infinitesimal shell and charge elements, respectively.

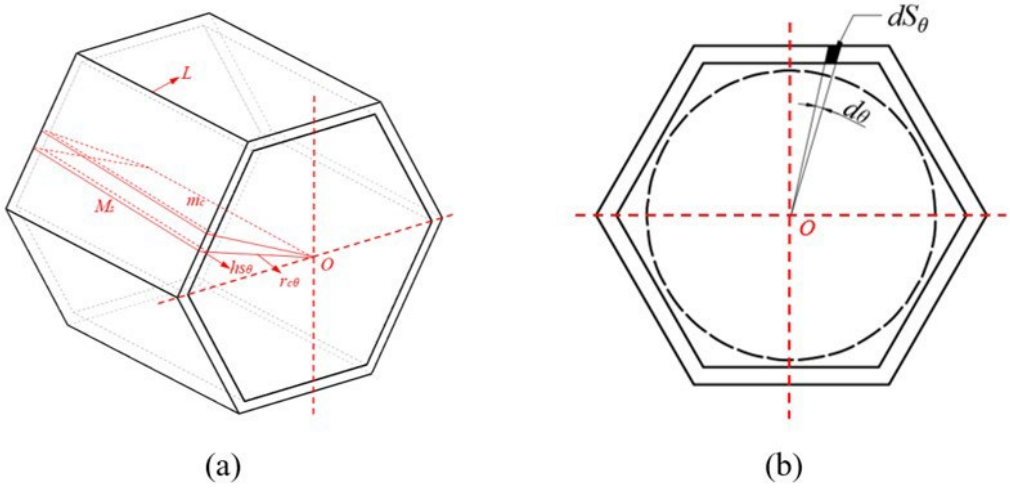

Figure 3 Hexagonal shell geometric model:(a)3D model, (b)Axial section.

The charge mass m and the shell mass M in formula (2) can be replaced by the microelement mass m_c and M_s respectively by assuming that each infinitesimal element moves independently. Under the polygonal charge structure, the change rule of charge diameter and shell thickness along the circumferential direction remains consistent. The angle k is solely determined by the minimum charge diameter D_{c0} and the shell thickness h_{s0}, thus it remains constant throughout the circumferential direction. By utilizing formulas (2) and (8) to (11), the angle k can be expressed as follows:

$$k = \frac{26.6^\circ}{\sqrt{2\frac{M_s}{m_c}+1}} = \frac{26.6^\circ}{\sqrt{4\frac{\rho_s h_{s0}}{\rho_c D_{c0}}+1}} \tag{12}$$

Figure 4 illustrates the effective charge shape under a typical hexagonal charge. In Figure 2-4 (a), the corresponding effective charge division is depicted for four circumferential angles. Figure 2-4 (b) provides a three-dimensional view of the effective charge. Although the angle k remains unchanged, the effective shape of the charge under the polygonal charge structure changes periodically along the circumferential direction due to the variation in charge diameter. This change resembles a hexagonal pyramid shape, resulting in a velocity gradient on the liner as well.

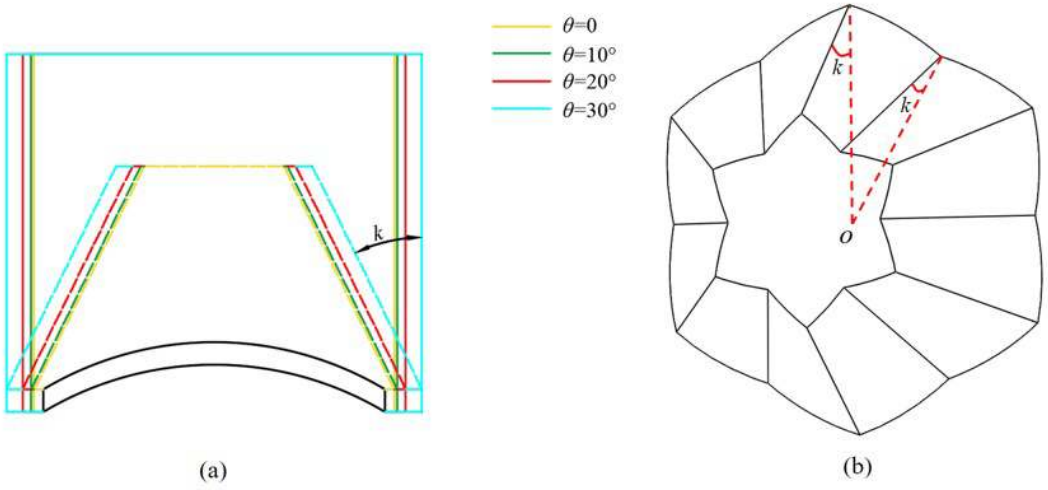

Figure 4 The effective charge shape under typical hexagonal charge. (a) 2D. (b) 3D.

2.3 Velocity distribution of liner under polygonal charge

As illustrated in Figure 5, the radial and axial components of the crushing velocity of the infinitesimal liner element, v_{xi} and v_{yi}:

$$v_{xi} = v_i \cos\alpha \tag{13}$$

$$v_{yi} = v_i \sin\alpha \tag{14}$$

where α represents the central angle of the infinitesimal liner element, i.e., the angle between the axis and the projection direction of the infinitesimal liner element.

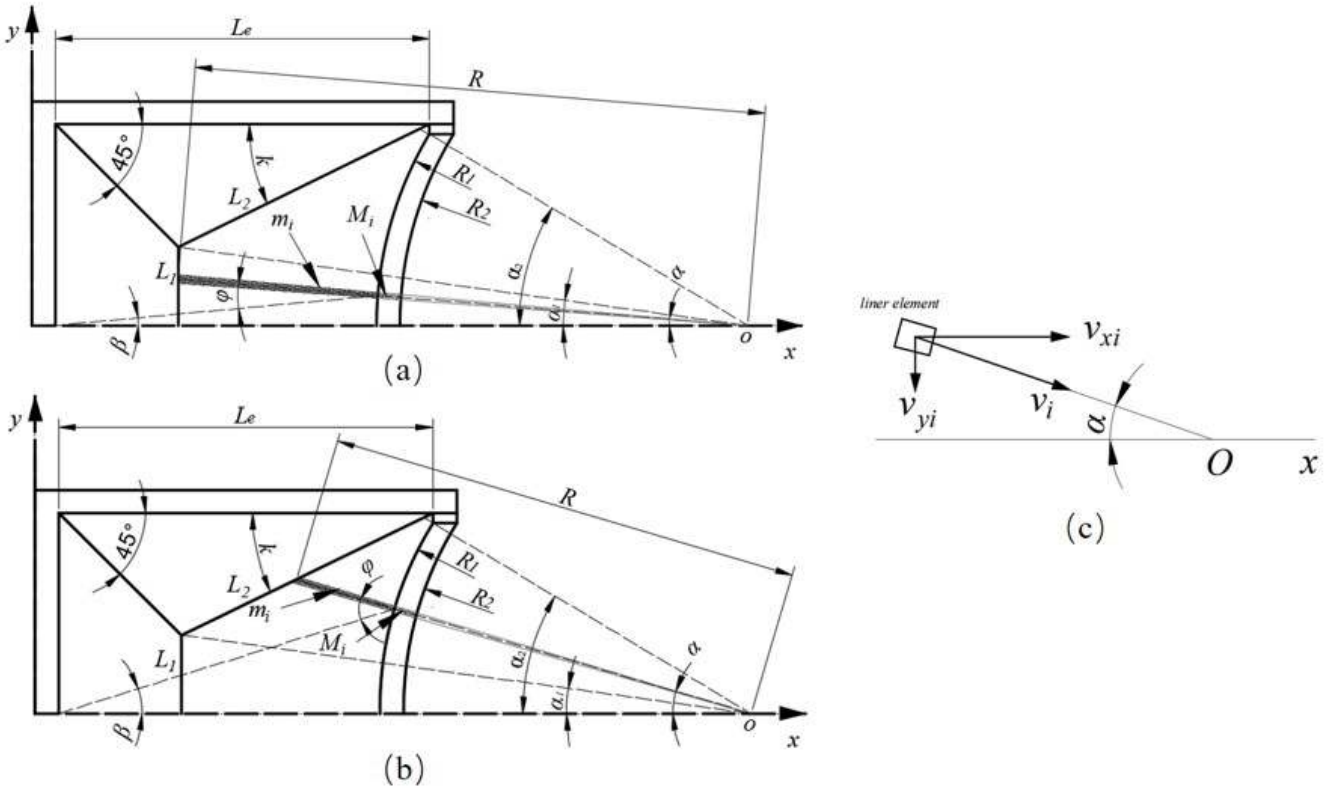

Figure 5 Schematic depicting the variables used to calculate the EFP velocity. (a) $\alpha<\alpha_1$, (b) $\alpha_1\leq\alpha\leq\alpha_2$, (c) velocity component calculation of liner element

At present, most of the research is based on the idea of micro-element method. The charge structure and liner structure are discretized and divided into n equal parts. The volume and mass of each equal part of the liner, effective charge and shell are solved in various ways. Then the formula (7) and formula (13) are solved to obtain the axial velocity corresponding to each equal part of the liner. Finally, according to the momentum conservation theorem and the mass conservation theorem, the EFP flight velocity, v_0 (Orilenko 2011, Sharma et al. 2001, Jeremić et al. 2017):

$$v_0 = \frac{\sum_{i=1}^{n} v_{ix} M_i}{\sum_{i}^{n} M_i}; i = 1, 2, \ldots, n \tag{15}$$

Then, in order to solve the velocity distribution, the mass condition under each infinitesimal element needs to be obtained using the method described above. The process of solving this is complex, and it becomes difficult to obtain the velocity distribution of the liner along the circumferential direction under a polygonal charge. The fundamental concept of integration is the sum of numerous infinitesimal elements. Based on formula (15), it is evident that the axial momentum of the liner is essentially the sum of the momentum of each infinitesimal element of the liner. Therefore, the concept of calculus can be introduced here to solve the problem of the liner's axial momentum.

Based on the infinitesimal integral, the equation for the axial momentum of the liner can be expressed as follows:

$$M_l v_0 = \rho_l V_l v_x = \iiint \rho_l v_{ix} dxdydz \tag{16}$$

where M_l is the mass of the liner, ρ_l is the density of the liner, V_l is the volume of the liner.

According to Figure 5, the axial momentum of the liner is solved more simply by using the spherical coordinate system. The rectangular coordinate system in Formula (16) is transformed into the spherical coordinate system as follows:

$$M_l v_0 = \iiint \rho_l v_{ix} r^2 \sin\alpha dr d\alpha d\sigma \tag{17}$$

In the equation, r, α and σ represent the distance, azimuth angle, and elevation angle respectively in the spherical coordinate system. The coordinate origin is taken as the reference point, with the center of the liner surface as the coordinate origin.

According to formula (7) and formula (13), formula (17) can be expressed as:

$$\begin{aligned} M_l v_0 &= \iiint \frac{\rho_l D}{8}(0.68+\cos\varphi) r^2 \sin\alpha\cos\alpha \cdot \frac{\rho_c}{\rho_l} dr d\alpha d\sigma \\ &= \frac{\rho_c D}{8}\int_0^{2\pi} d\sigma \int_0^{\alpha_2} (0.68+\cos(\alpha+\beta))\sin\alpha\cos\alpha d\alpha \int_{R_1}^{R} r^2 dr \end{aligned} \tag{18}$$

where α_2 is the maximum central angle corresponding to the effective charge micro-element, that is, the maximum elevation angle in the spherical coordinate system, β is the angle between the line connecting the cover micro-element and the detonation point and the axial direction, and R is the distance from the edge line to the center of the effective charge, R_1 is the liner radius of outer curvature.

As shown in Figure 5, when the liner and the effective charge arcs are divided into n elements, each liner element corresponds to a different central angle. The central angle, α_1, which corresponds to the intersection of effective charge lines L_1 and L_2, is referred to as the critical central angle. Thus, the division of the liner and the effective charge comprises three stages. When $\alpha<\alpha_1$, the effective charge volume corresponding to the liner element is calculated according to the effective charge line L_1 (as shown in Figure 5(a)). When $\alpha_1\leq\alpha\leq\alpha_2$, the effective charge volume corresponding to the liner element is calculated according to the effective charge line L_2 (as shown in Figure 5(b)). And when $\alpha>\alpha_2$, the liner element does not directly contact the effective charge, so it is not significantly affected by the impact load or the load is minimal. In this stage, the axial momentum is ignored. Therefore, the axial momentum of the first two stages of the liner can be represented as follows:

$$M_1 v_{x1} = \frac{\rho_c D\pi}{12}\int_0^{\alpha_1} (0.68+\cos(\alpha+\beta))\sin\alpha\cos\alpha(R^3-R_1^3)d\alpha \tag{19}$$

$$M_2 v_{x2} = \frac{\rho_c D\pi}{12}\int_{\alpha_1}^{\alpha_2} (0.68+\cos(\alpha+\beta))\sin\alpha\cos\alpha(R^3-R_1^3)d\alpha \tag{20}$$

In Equations (18) and (19), M_1 and M_2 are the mass of the liner in two stages respectively, and v_{x1} and v_{x2} are the velocity of the liner in two stages respectively.

In this study, α_1, α_2, and β were calculated using Equations (21), (22), and (23), respectively:

$$\alpha_1 = \arctan\left(\left[\frac{D_c}{2} - \frac{L_e}{1+\tan(\pi/2-k)} \right] \Big/ \left[\frac{L_e \tan(\pi/2-k)}{(1+\tan(\pi/2-k))} + \sqrt{R_1^2 - \frac{D_l^2}{4}} \right] \right) \tag{21}$$

$$\alpha_2 = \arcsin(D_l / 2R_1) \tag{22}$$

$$\beta = \arctan\left(\frac{R_1 \sin\alpha}{L_e + \sqrt{R_1^2 - \frac{D_l^2}{4}} - R_1 \cos\alpha} \right) \tag{23}$$

where L_e represents the distance from the liner edge to the initiation end of the charge.

R varies with the central angle differently during the two stages, as expressed by Equations (24) and (25):

$$R = \begin{cases} \left[\frac{L_e \tan(\pi/2-k)}{(1+\tan(\pi/2-k))} + \sqrt{R_1^2 - \frac{D_l^2}{4}} \right] \Big/ \cos\alpha & \alpha \le \alpha_1 \\ c \sin(k+\alpha_1) / \sin(k+\alpha) & \alpha_1 < \alpha \le \alpha_2 \end{cases} \tag{24}$$

$$c = \left[\frac{L_e \tan(\pi/2-k)}{(1+\tan(\pi/2-k))} + \sqrt{R_1^2 - \frac{D_l^2}{4}} \right] \Big/ \cos\alpha_1 \tag{25}$$

Assuming that the effects of the detonation products are negligible during the inertial deformation stage of the EFP. Without considering the fracture of the liner, the EFP flight velocity, v_0, can be obtained from the axial velocity of the infinitesimal liner element based on the laws of momentum and mass conservation:

$$v_0 = \frac{M_1 v_{x1} + M_2 v_{x2}}{M_1 + M_2 + M_3} = \frac{M_1 v_{x1} + M_2 v_{x2}}{M_l} \tag{26}$$

In Equation (26), M_3 represents the mass of the liner under the third stage.

To validate the accuracy of theory, experimental values from the literature (Huang et al. 2023, Hussain et al. 2013, Li et al. 2003, Yang and Lin 2021, Wang et al. 2016) were selected and compared with the corresponding theoretical calculation values, as depicted in Figure 6. The results reveal a strong agreement between the theoretical and experimental values, with a deviation of less than 5%. This finding serves to confirm the efficacy of Equation (26) in accurately determining the EFP flight velocity.

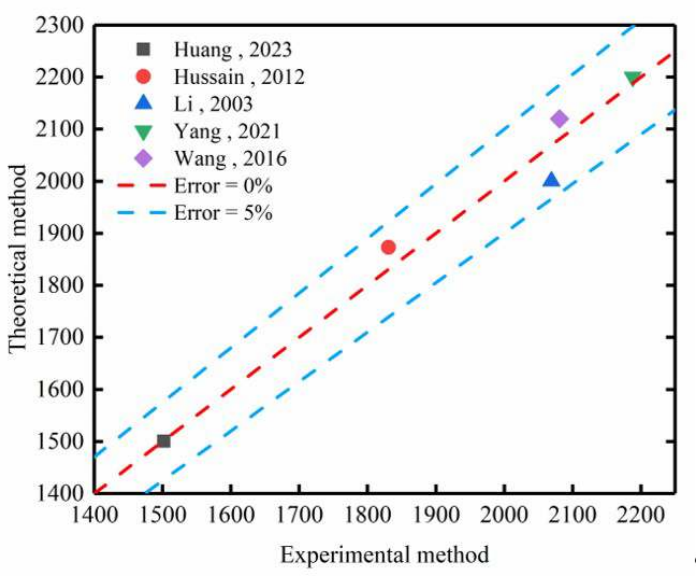

Figure 6 Error comparison between theoretical calculation value and experimental value

The variables in the momentum calculation equation are the central angles of the two stages, α_1 and α_2, which, according to Equations (21) and (22), are solely dependent on the charge diameter for a given liner with known diameter and radius of curvature values. For a polygonal charge, the liner velocity distribution in the circumferential direction can be obtained:

$$v_0(\theta) = \frac{M_1(\theta)v_{x1}(\theta) + M_2(\theta)v_{x2}(\theta)}{M_l} \tag{27}$$

In Equation (27), ϑ is the central angle of the liner along the circumferential direction, $v_0(\vartheta)$ is the axial velocity distribution of the liner along the circumferential direction, and $M_1v_{x1}(\vartheta)$ and $M_1v_{x2}(\vartheta)$ are the axial momentum of the liner along the circumferential distribution in the two stages, respectively.

The section shape of the main charge is an inscribed regular hexagon with a diameter of 70 mm, and the hexagonal charge with a charge height of 60 mm is taken as a typical example. The velocity distribution along the circumferential direction of the liner element is obtained as shown in Figure 7. In the case of a polygonal charge structure, the formation of the tail wing EFP can be attributed to the variation in effective charge along the circumferential direction of the linear element, leading to different crushing speeds under the explosion load. At larger charge diameters, the crushing speed of the linear element is higher, causing the edge of the liner to protrude forward and form the tail fins of EFP.

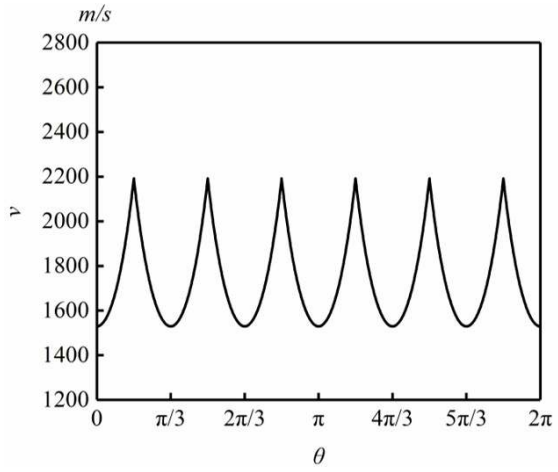

Figure 7 The velocity distribution of the liner microelement under typical hexagonal charge

3 NUMERICAL SIMULATION AND TEST OF EFP WITH TAIL FINS FORMATION

3.1 Finite element (FE) computational method

3.1.1 Computational model

The EFP formation characteristics were computed using the arbitrary Lagrangian–Eulerian method (Yang and Lin 2021). The explosive and air parameters were computed using a multi-material Eulerian algorithm. The liner and shell parameters were computed using a Lagrangian algorithm. The interactions between the Eulerian and Lagrangian elements were solved using a fluid–solid coupling algorithm. The tail fin EFP formation was numerically simulated using the LS-DYNA software. To accurately simulate tail fin EFP formation using a polygonal charge, a full model of the charge was developed. The mesh size was 0.5–0.8 mm. To prevent pressure from reflecting from the boundary plane and transferring through the liner meshes, the air boundary in the computational domain was defined as non-reflecting and the liner boundary was defined as automatic surface contact. Figure 8(a) shows the overall FE computational model, and Figure 8(b) shows the FE model for the liner.

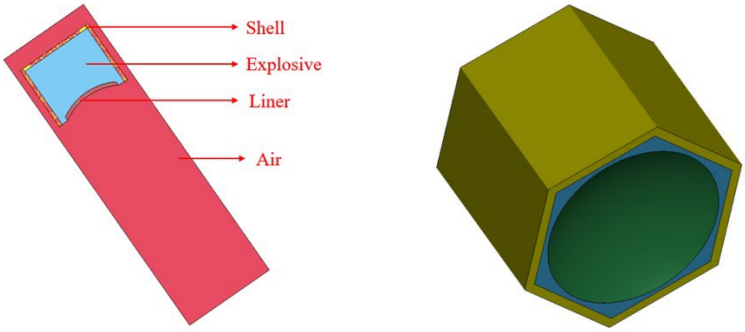

Figure 8 FE computational model: (a) FE model of the entire computational domain and (b) FE model of the shaped charge.

3.1.2 Material model and parameters

A JH-2 explosive was used, and it was described using the HIGH_EXPLOSIVE_BURN constitutive model and the Jones–Wilkins–Lee equation of state, which can be mathematically expressed by Equation (28) (Liu et al. 2017):

$$\mathrm{p} = A_1\left(1-\frac{\omega}{R_1V}\right)e^{-R_1V} + B_1\left(1-\frac{\omega}{R_2V}\right)e^{-R_2V} + \frac{\omega e}{V} \tag{28}$$

In Equation (28), p represents the pressure in the explosive element at the current moment, V is the specific volume, e is the initial specific internal energy, and A_1, R_1, B_1, R_2, and ω are the parameters of the explosive.

The liner and shell were made from red copper and aluminum, respectively. To express their impact hardening, temperature softening, and strain rate behaviors under the explosive load, both components were described using the Johnson–Cook constitutive model and the Gruneisen equation of state. The Johnson–Cook constitutive model can be mathematically expressed by Equation (29) (Johnson and Cook 1983):

$$\sigma = \left(\sigma_0 + B\varepsilon^{\mathrm{n}}\right)\left(1 + C\ln\frac{\dot{\varepsilon}}{\dot{\varepsilon}_0}\right)\left(1 - T^{*\mathrm{n}}\right) \tag{29}$$

where σ is the equivalent stress of the material, A represents the yield stress at the reference strain rate and temperature, B is the strain hardening coefficient, ε is the equivalent plastic strain, n is the strain hardening index, C is the strain rate correlation coefficient, $\dot{\varepsilon}_0$ represents the reference strain rate, $\dot{\varepsilon}$ is the actual strain rate, $T^* = \frac{T-T_r}{T_m-T_r}$ is the similarity temperature, T_m is the melting temperature of the material, T_r is the reference temperature, T is the transient temperature, and m is the temperature correlation coefficient.

Tables 1 and 2 list the parameters of the explosive and of the liner and shell, respectively.

Table 1 Parameters of the explosive (Liu et al. 2022)

ρ (g/cm3)	Dc (m/s)	PC-J (GPa)	A (GPa)	B (GPa)	R1	R2	ω	E0 (GPa)
1.70	8,425	29.66	854.5	20.49	4.6	1.35	0.25	18.5

Table 2 Material parameters for the liner and the shell (Johnson and Cook 1983)

	ρ (g/cm3)	A (MPa)	B (MPa)	n	c	M
Copper	8.96	90	292	0.31	0.025	1.09
Aluminum	2.77	265	426	0.34	0.015	1.0

3.2 Recovery test setup

Given that tail fin EFP formation cannot be completely characterized by two-dimensional X-ray images, soft recovery tests were performed using a continuous array of blocks made of soft materials with increasing densities (Fu et al. 2022). The polygonal EFP warhead used in this study consisted of a top cover, a shell, a liner, an explosive, and a detonator. Figure 9 shows the charge structure. The cross-sectional shape of the charge body was an equilateral hexagon circumscribed by a 70-mm-diameter circle. A JH-2 explosive with a charge height of 60 mm and a charge density of 1.70 g/cm^3 was used. A hemispherical (radius of curvature = 56 mm) red copper liner with a uniform thickness was used, and it was distressed before charging. The top cover and shell had matching polygonal structures, were made from aluminum, and had minimum thicknesses of h_{s0} = 3 mm.

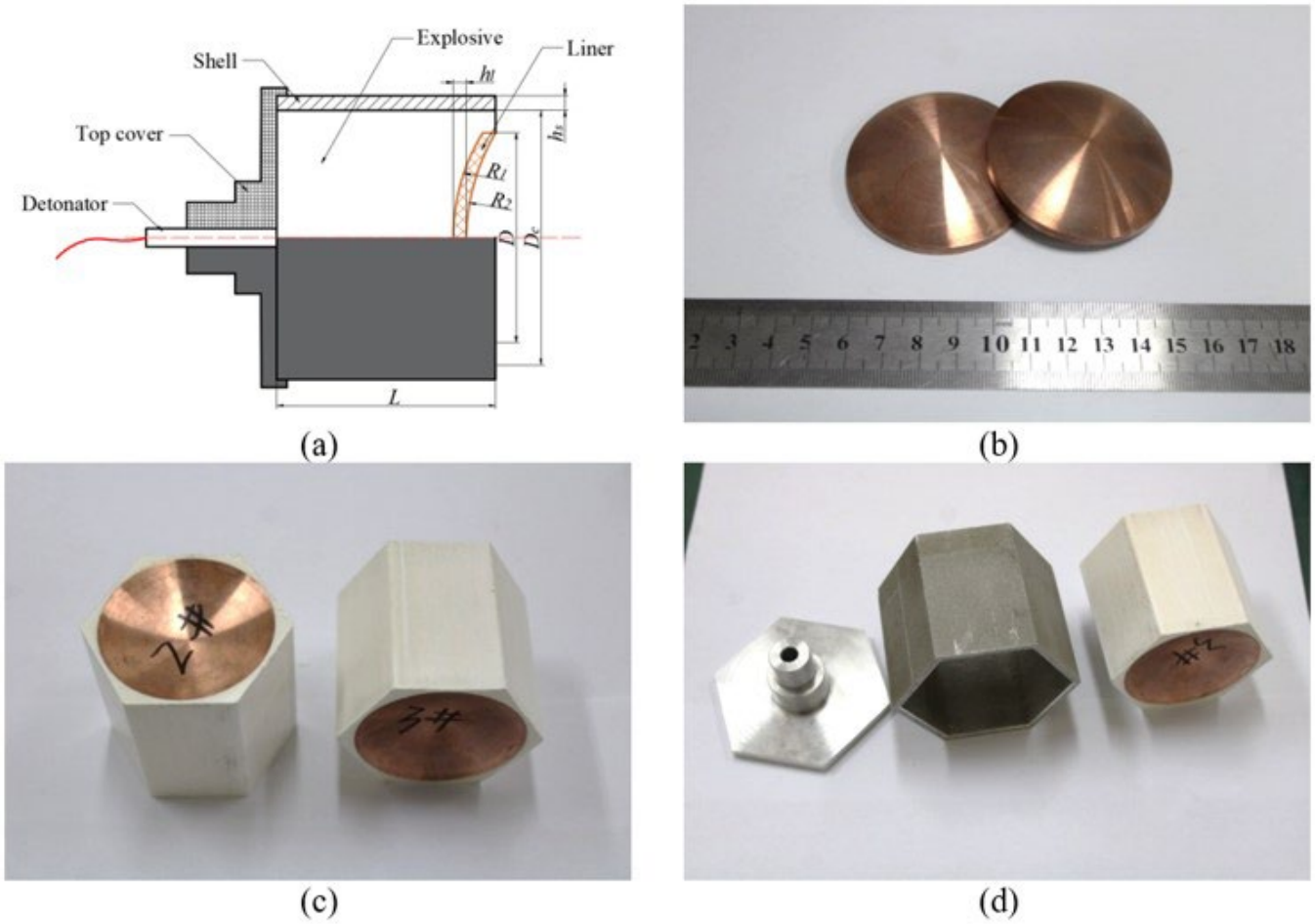

Figure 9 Charge structure: (a) 2D geometric model, (b) liners, (c) charges without shells, and (d) charge and accessory components (shell and top cover).

The blocks were made from polystyrene foam (density = 0.02 g/cm^3), polyurethane foam plates of different densities (0.04 and 0.06 g/cm^3), expanded vermiculite (density = 0.15 g/cm^3), sawdust (density = 0.22 g/cm^3), and fiber plates (0.5 g/cm^3). The sawdust and fiber plates were placed in wooden boxes with dimensions of 1 m × 1 m × 1 m. The blocks were arranged in a continuous array that had a total length of 12 m, as shown in Figure 10. The two polyurethane blocks, the vermiculite box, the sawdust box, and the fiber plate block had lengths of 3 m, 2 m, 3 m, 2 m, and 1 m, respectively. Three EFP shots were fired and recovered; two shots were fired with a shell and one was fired without a shell. The EFP charges were placed on a wooden stand approximately 3 m from the first recovery block, and the charge axis was positioned parallel to the ground. Table 3 lists the material specifications and geometric parameters of the soft blocks used in the EFP recovery tests.

Table 3 Soft recovery material parameters

Type	Cross-sectional dimensions(m)	Material	Density(g/cm3)	Length(m)
1	1 × 1	Polystyrene foam	0.02	2
2	1 × 1	Polyurethane foam	0.04	3
3	1 × 1	Polyurethane foam	0.06	2
4	1 × 1	Expanded vermiculite	0.18	2
5	1 × 1	Sawdust	0.30	2
6	1 × 1	Fiber plate	0.50	1

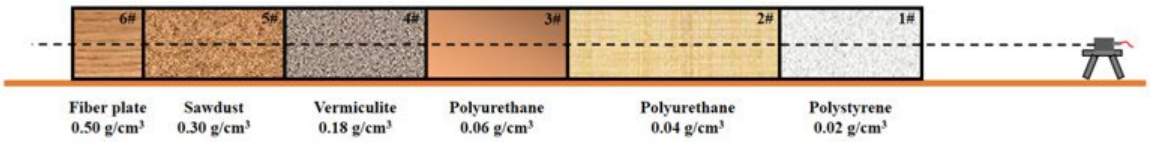

(a)



(b)

Figure 10 Test setup: (a) schematic diagram and (b) photograph.

3.3 Results and discussion

3.3.1 Tail fin formation process

The process of forming a tail fin EFP using a polygonal charge is discussed next. For the hexagonal charge, the explosion begins at t = 0 and the spherical detonation wave propagates toward the liner. When the detonation wave impacts the liner, the center of the liner accelerates before the edge, and the edge starts curling outward. During the time interval from *t* = 30 μs to t = 60 μs, the axial and radial velocities produced by the detonation wave vary among the infinitesimal liner elements at different radial positions, and the liner deforms to form tail fins. At t = 90 μs, tail fins form and begin to contract inward while the EFP continues to stretch. At t = 150 μs, the shape of the EFP has essentially stabilized. Figure 11 depicts the tail fin EFP formation process. The deformation of the tail fin EFP is minimal after 150 μs and is therefore not presented in the figure.

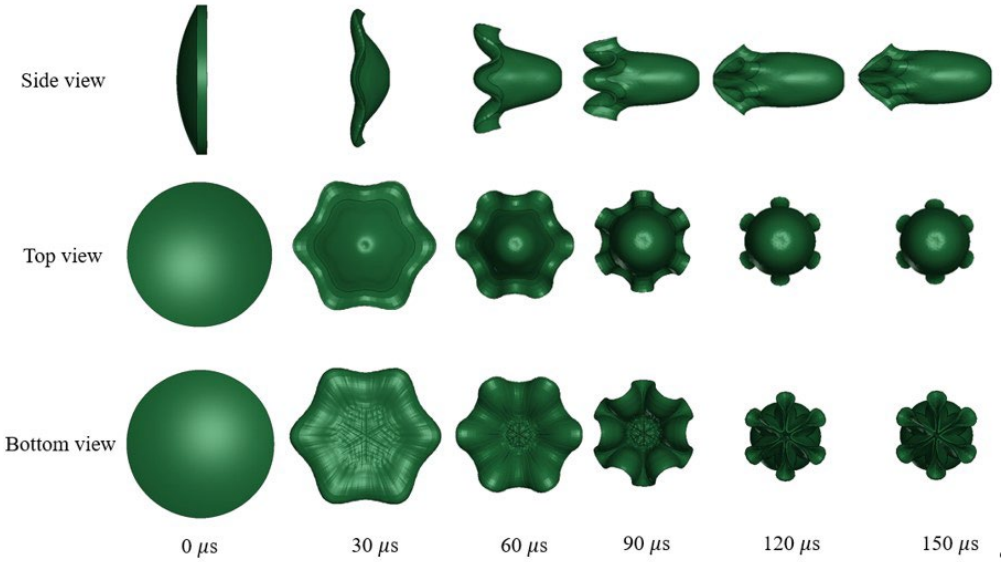

Figure 11 Tail fin EFP formation process.

The changes in circumferential velocity of the liner are compared between the liner under the hexagonal charge structure and the liner under the two conventional cylindrical charge structures at 10 ~ 25 μs, with the charge diameter of the cylindrical structures is equal to the charge diameter of ϑ = 0 ° and ϑ = 15 ° under the hexagonal charge structure, as illustrated in Figure 12. Upon detonation, the liner undergoes deformation due to the detonation load. At 10μs, the circumferential distribution of the liner velocity under the hexagonal charge structure starts to exhibit periodicity, with the liner element corresponding to the larger charge diameter displaying a higher velocity, resembling a hexagonal pattern. This can be attributed to the fact that adjacent liner elements experience varying impact loads, resulting in a velocity gradient. In contrast, the liners under the two conventional cylindrical charges only exhibit a uniform velocity distribution in the circumferential direction under the impact of the detonation load. Notably, when the charge diameter is large, the central velocity range of the liner is significantly greater than that of the smaller charge diameter, which is consistent with the results caused by the effective charge division.

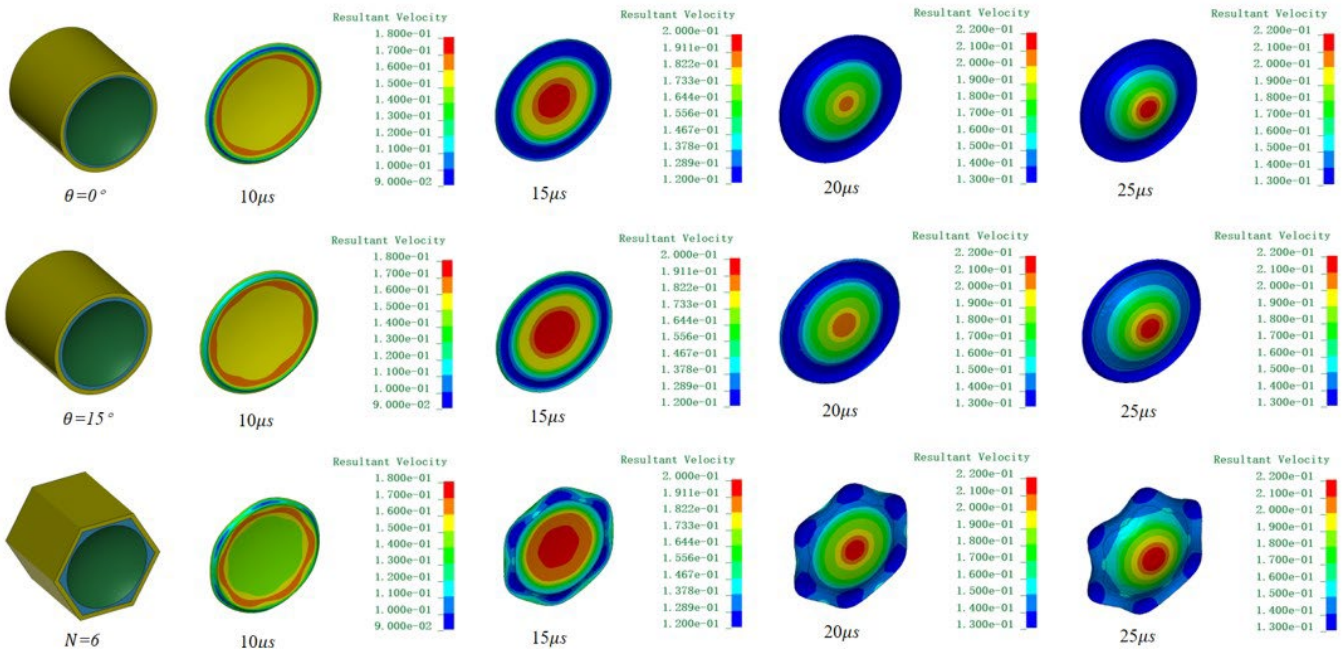

Figure 12 The velocity distribution of the liner along the circumferential direction at early times under the initial detonation load under three charge structures

Figure 13(a) shows the velocity–time curves of the infinitesimal liner elements for a half cycle within the first 180 μs after detonation and the theoretically calculated velocity curve of the hexagonal charge. Figure 13(b) the velocity distribution along the circumferential direction of the liner edge at three specific moments. Because of the interactions between the infinitesimal liner elements during the deformation, the differences between the velocities of the infinitesimal elements along the circumferential edge of the liner decreased with time (from 10 to 80 μs). Tail fins were formed and stabilized after 80 μs, the velocity order of the liner element will undergo certain changes and fluctuate back and forth to some extent, eventually tending towards stability. Figure 13(b) clearly depicts the periodic velocity changes of the liner edge along the circumferential direction. Specifically, the velocity change curve at the edge of the liner during the initial stage at 40 μs closely matches the theoretical prediction. In contrast to the changes observed at 40μs and 155μs, the trend of the linear element at 100μs is opposite. This can be attributed to the interaction between the linear elements and the speed variations resulting from their mutual involvement in the deformation process. The final velocity of the EFP calculated using the theoretical curve according to the theorem of the conservation of axial momentum (1740 m/s) was consistent with the uniform velocity after the end of the deformation stage (at t = 180 μs) obtained from numerical simulation computations (1660 m/s). The difference between the two velocities was 4.8%.

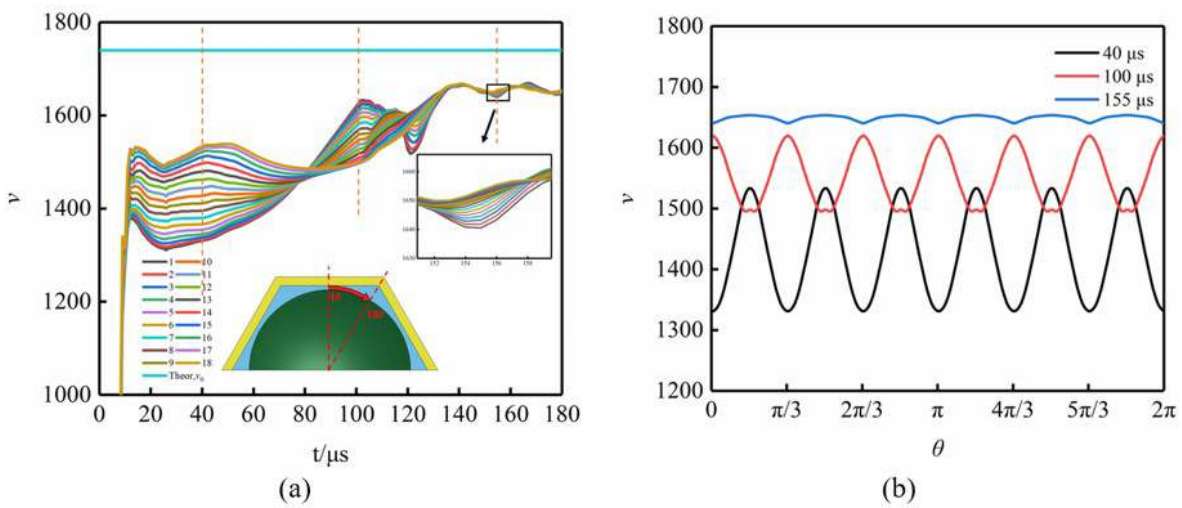

Figure 13 Liner velocity distributions: (a) circumferential liner velocity variations within a half cycle, and (b) theoretical circumferential liner velocity variations.

3.3.2 Comparison of test and simulation results

Figure 14(a) and (b) present the experimental results for the two EFP shots fired using the charge shown in Figure 9(d). According to the test results of two shelled hexagonal EFP warheads, for the first shot, the EFP had almost no residual velocity after penetrating the top of the first sawdust-filled wooden box and was recovered outside of the box. The tail of the EFP was partially broken due to collision with the wooden box panels, and the separated part was recovered from the top panel of the wooden box. The connection between the tail and the main body of the EFP was dented due to high-speed collisions with the various media, as shown in Figure 14(a). After the second shot, the EFP was recovered from the first sawdust-filled wooden box. The high-speed collisions between the copper EFP and the recovery materials inevitably caused losses in mass and broken tail fins. The initial liner mass was 87.74 g for both EFP warheads, while the masses of the recovered EFPs were 84.30 g and 84.34 g. The mass recovery rate exceeded 96%, thereby satisfying the required EFP recovery.

Figure 14(c) is the experimental results of charge structure without shell in Figure 9(c). As the evidenced by recovered EFPs in Figures 14(a), (b) and (c), it can be found that although the tail of the formed EFP shrinks seriously in the case of no shell, resulting in a smaller tail diameter, there are also six clearly visible tails. Therefore, tail fin EFPs were formed using the hexagonal charges, regardless of whether there was a shell, this result confirms the feasibility of forming tail fin EFPs using polygonal shaped charges. The geometries of the recovered EFPs formed by the charges with shells were compared with that of a numerically simulated EFP. Table 4 shows the structural parameters of the EFPs formed by the charges with shells. The average length of the two EFPs was 46.4 mm, while the length of the simulated EFP was 48.4 mm. Thus, the error was less than 4.3%. The average maximum diameter of the two EFPs was 20.2 mm, while that of the simulated EFP was 20.3 mm; this represents an error of less than 0.5%. Since the differences between the geometric parameters of the experimentally obtained EFPs and the simulated EFP were relatively small, the accuracy of the numerically simulated tail fin EFP was verified.

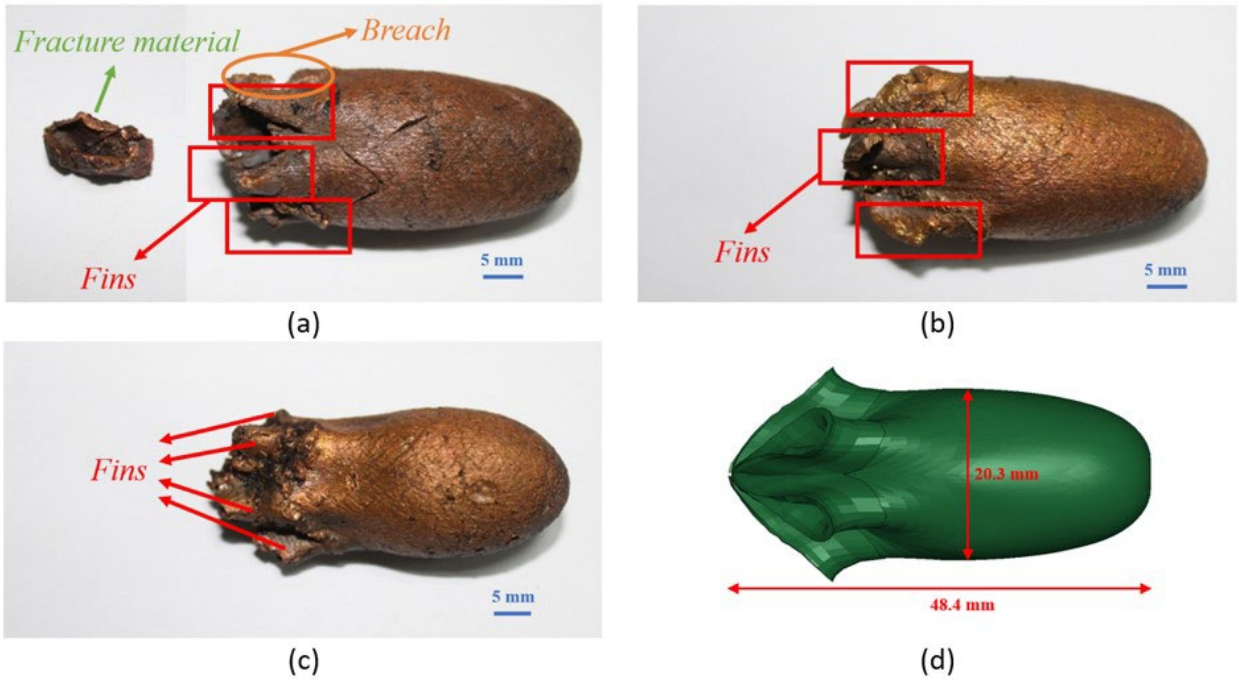

Figure 14 Experimental and simulation results: (a) shot 1# (with shell), (2) shot 2# (with shell), (c) shot 3# (without shell), and (d) numerical simulation results (with shell).

Table 4 Comparison of the simulation and experimental results

Method	Length	Maximum diameter	Length-to-diameter ratio
Experimental results (mean)	46.4 mm	20.2 mm	2.30
Simulation results	48.4 mm	20.3 mm	2.38
Difference	4.3%	0.5%	3.4%

4 Formation behavior of tail fin EFPs Created using polygonal charges

4.1 Characteristic parameters of tail fin EFPs

A tail fin EFP can be divided into two parts: the head (main body) and the tail (Liu et al. 2014b). The head is solid, while the tail is hollow. Figure 15 shows the structural parameters of a tail fin EFP. In this paper, v represents the EFP velocity, D_E is the maximum diameter of the head, L_E is the length of the entire projectile, L_M is the length of the solid portion of the EFP, L_E/D_E is the length-to-diameter ratio, W_E is the tail diameter (the largest length between the tips of opposite fins), W_E/D_E is the tail-to-head diameter ratio, and μ represents the compactness of the EFP and is equal to L_M/L_E.

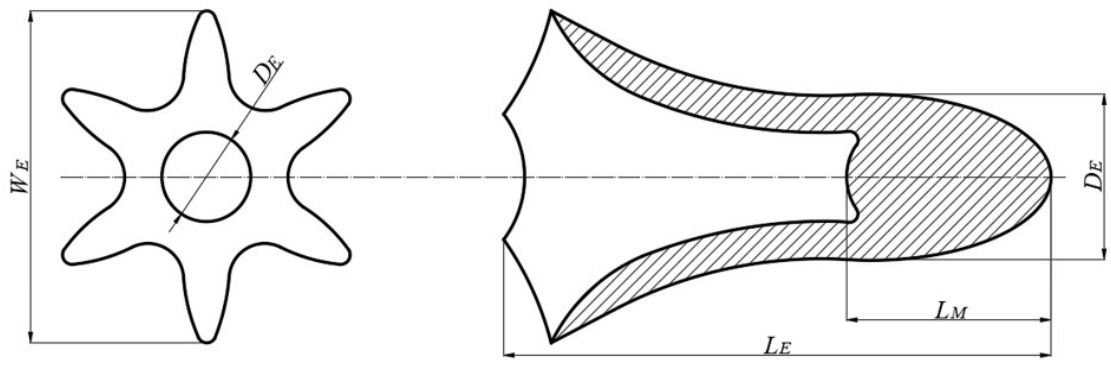

Figure 15 Illustration of the structural parameters of a tail fin EFP.

4.2 Effects of the structural parameters of the hexagonal charge on the performance of the resulting tail fin EFP

Understanding the effects of the structural parameters of polygonal charge on the performance of the resulting tail fin EFPs is critical to the design and optimization of EFP warheads formed using polygonal charges. The effects of the liner radius of curvature, R_1 and R_2, the thickness, h_l, the charge height, L, and the shell thickness, h_{s0}, on the formation behavior of a tail fin EFP created using the hexagonal charge were investigated using numerical simulations. The performance of the tail fin EFP was evaluated using several measures, including the EFP velocity, v, the length-to-diameter ratio, L_E/D_E, the compactness, μ, and the tail-to-head diameter ratio, W_E/D_E.

4.2.1 Effects of liner radius of curvature on tail fin EFP formation

The formation of tail fin EFPs was calculated for different values of the liner radius of curvature, R_1 (which increased from $0.7D_c$ to $0.9D_c$ by increments of 3.5 mm), and constant parameter values of D_c = 70 mm, h_l = 3.8 mm ($0.0543D_c$), $L = 0.85D_c$, $h_{s0} = 0.06D_c$, and $R_2 = R_1$. Figure 16 shows the geometric parameters and morphologies of the tail fin EFPs at t = 180 μs that were formed using a polygonal charge and different R_1 values.

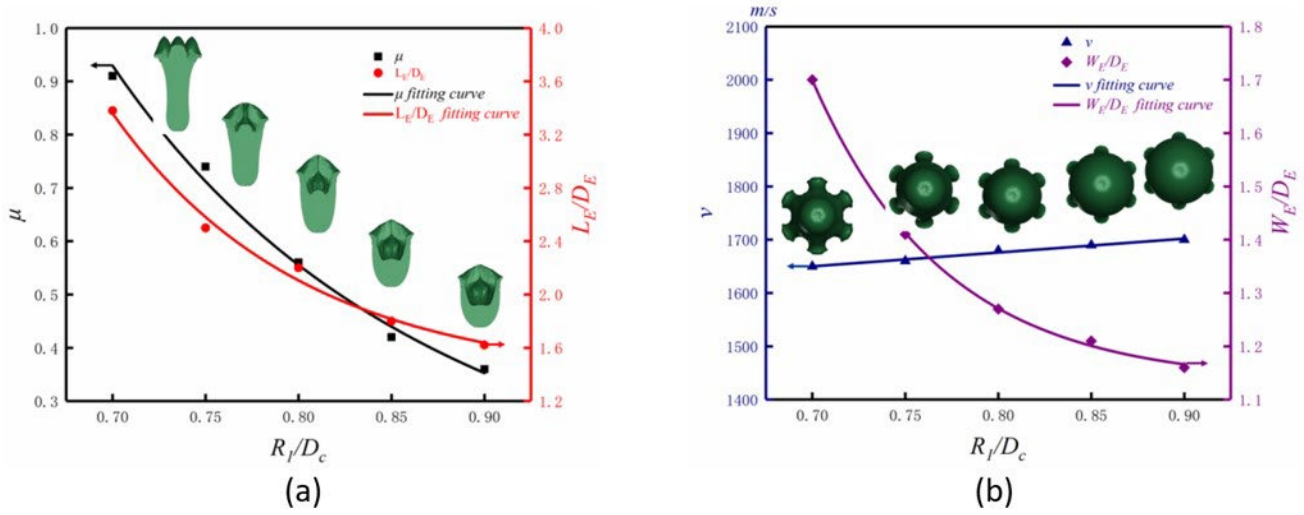

Figure 16 Variations in geometric tail fin EFP parameters with R_1: (a) variations in μ and L_E/D_E with R_1 and (b) variations in v and W_E/D_E with R_1.

As shown in Figure 16, as R_1 increased from $0.7D_c$ to $0.9D_c$, L_E/D_E decreased quasi-linearly, μ and W_E/D_E decreased such that they were approximately power functions of R_1, and v increased linearly with a small slope. In addition, as R_1 increased, the liner deformation mode changed from crushing to bending, the EFP did not stretch adequately, and the head diameter was excessively large; these results led to decreases in the length-to-diameter ratio, the compactness, and the tail-to-head diameter ratio (the tail diameter did not change substantially with R_1, while the head diameter increased). Further, as R_1 increased, the amount of charge also increased, and hence the EFP velocity increased slightly. In summary, when R_1 was excessively small, the center of gravity was located toward the rear of the EFP (which was detrimental to the EFP flight performance), and the head had a constricted neck that was prone to fracture. When R_1 was excessively large, the EFP compactness and tail-to-head diameter ratio were small, thereby reducing the penetration power and flight stability. Therefore, the optimal value of R_1 was determined to be in the $0.75D_c$–$0.85D_c$ range.

4.2.2 Effects of liner thickness on tail fin EFP formation

The formation of tail fin EFPs was calculated for different values of the liner thickness, h_l (which increased from 3.0 mm to 4.6 mm ($0.0429D_c$–$0.0657D_c$) by increments of 0.4 mm), and constant parameter values of D_c = 70 mm, $R_1 = R_2 = 0.8D_c$, $L = 0.85D_c$, and $h_{s0} = 0.06D_c$. Figure 17 shows the geometric parameters and morphologies of the tail fin EFPs at t = 180 μs that were formed using a polygonal charge and different h_l values.

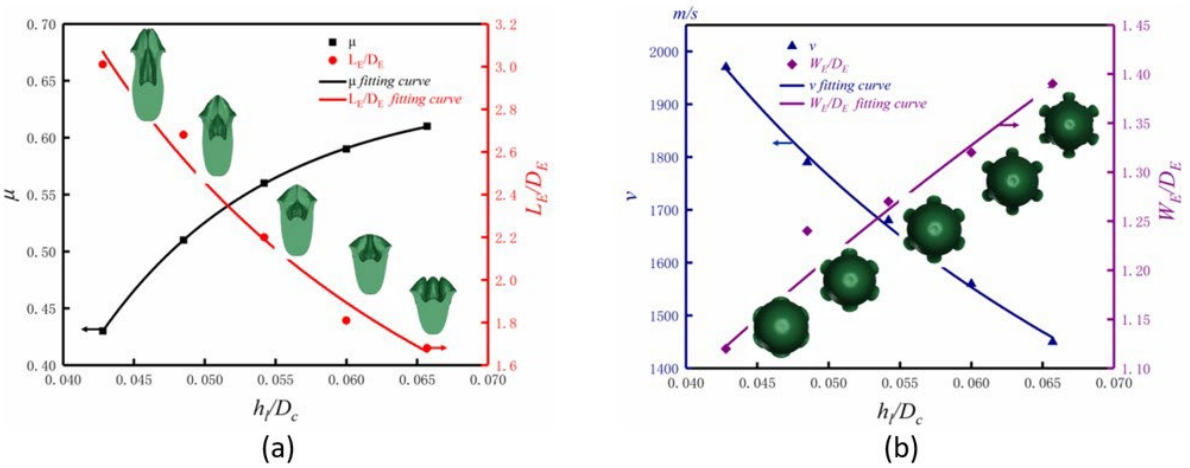

Figure 17 Variations in geometric tail fin EFP parameters with h_l: (a) variations in μ and L_E/D_E with h_l and (b) variations in v and W_E/D_E with h_l.

Figure 17 shows that the liner mass increased as h_l increased from 3.0 to 4.6 mm, that v and L_E/D_E decreased such that they were approximately power functions of h_l, and that μ and W_E/D_E increased such that they were approximately power functions of h_l. When h_l was excessively small, the EFP had a high velocity but an excessively large length-to-diameter ratio and a constricted neck that was prone to fracture. When h_l was excessively large, the EFP had a low velocity and a small length-to-diameter ratio; thus, it also had a low penetration power. Therefore, the optimal value of h_l was determined to be in the 3.4–4.2 mm range ($0.0486D_c$–$0.06D_c$).

4.2.3 Effects of charge height on tail fin EFP formation

The formation of tail fin EFPs were calculated for different values of the charge height, L (which increased from $0.65D_c$ to $1.05D_c$ by increments of 7 mm), and constant parameter values of D_c = 70 mm, $R_1 = R_2 = 0.8D_c$, h_l = 3.8 mm ($0.0543D_c$), and $h_{s0} = 0.06D_c$. Figure 18 shows the geometric parameters and morphologies of the tail fin EFPs at t = 180 μs that were formed using a polygonal charge and different values of L.

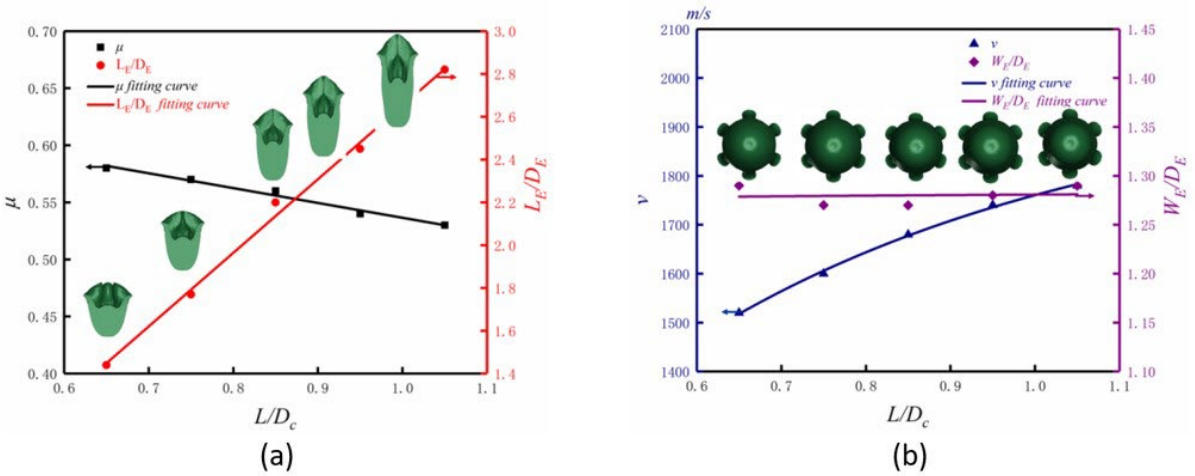

Figure 18 Variations in geometric tail fin EFP parameters with L: (a) variations in μ and L_E/D_E with L and (b) variations in v and W_E/D_E with L.

Figure 18 shows that, as L increased from $0.65D_c$ to $1.05D_c$, v and L_E/D_E increased such that they were approximately power functions of L, μ decreased, and W_E/D_E remained nearly constant. When $L > 1.05D_c$, the tail fin EFP had a high velocity and a large length-to-diameter ratio but was excessively stretched and prone to fracture. When $L < 0.75D_c$, the tail fin EFP had an excessively low velocity and a small length-to-diameter ratio; thus, it also had a low penetration power. Therefore, to form an EFP with a high velocity, a large length-to-diameter ratio, and a large tail-to-head diameter ratio while decreasing the fracture risk, the optimal value of L was determined to be in the $0.75D_c$–$1.05D_c$ range.

4.2.4 Effects of shell thickness on tail fin EFP formation

The formation of tail fin EFPs were calculated for different values of the shell thickness, h_{s0} (which increased from $0.04D_c$ to $0.12D_c$ by increments of 1.4 mm), and constant parameter values of D_c = 70 mm, $R_1 = R_2 = 0.8D_c$, h_l = 3.8 mm ($0.0543D_c$), and $L = 0.85D_c$. Figure 19 shows the parameters of the tail fin EFPs at t = 180 μs that were formed using a polygonal charge and different hs_0 values.

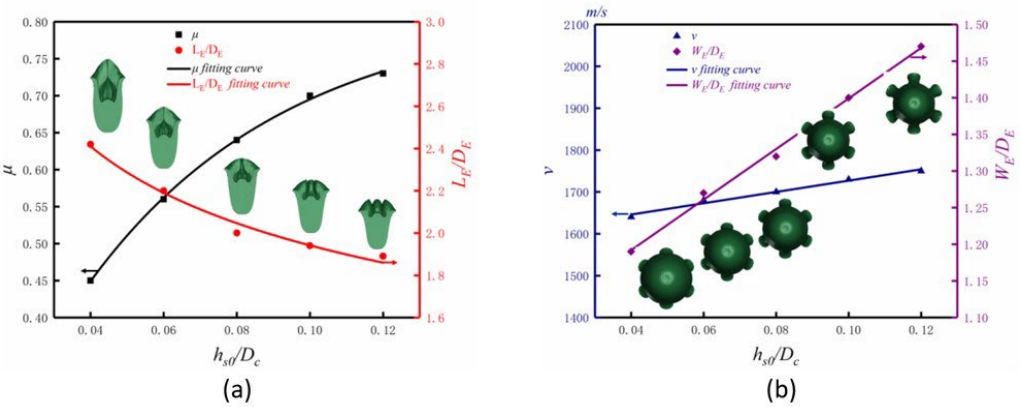

Figure 19 Variations in geometric tail fin EFP parameters with h_{s0}: (a) variations in μ and L_E/D_E with h_{s0} and (b) variations in v and W_E/D_E with h_{s0}.

Figure 19 shows that, as h_{s0} increased from $0.04D_c$ to $0.12D_c$, v, μ, and W_E/D_E increased, while L_E/D_E decreased such that it was approximately a power function of h_{s0}. When $h_{s0} > 0.10D_c$, the tail fin EFP had a small length-to-diameter ratio and a low penetration power. When $h_{s0} < 0.06D_c$, the tail fin EFP had excessively low velocity, compactness, and tail-to-diameter ratio values, which led to a low penetration power and poor flight stability. Therefore, to form tail fin EFPs with high velocity, length-to-diameter ratio, and compactness values while ensuring acceptable flight stability, the optimal value of h_{s0} was determined to be in the $0.06D_c$–$0.10D_c$ range.

4.3 Numerical simulation of the formation of tail fin EFPs while using different polygonal charges

Numerical simulations and experimental results have indicated that a hexagonal charge is capable of forming an EFP with six fins, a good morphology, and a high velocity. To further investigate the feasibility of forming tail fin EFPs using polygonal charges, the formation of tail fin EFPs was numerically simulated for rectangular, hexagonal, octagonal, and decagonal charges designed based on the charge structural parameters used in the experiment performed during this study (with the subcaliber charge thickness, t_0, and minimum shell thickness, h_{s0}, values held constant).

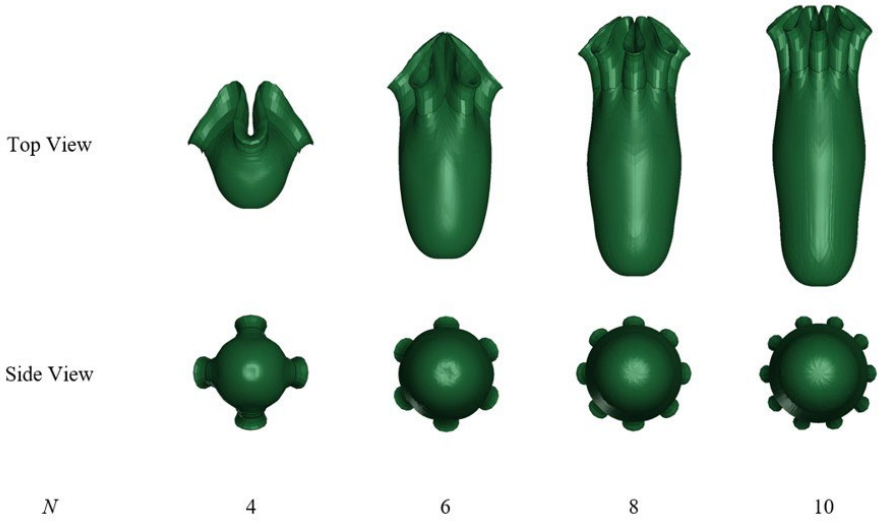

Figure 20 the morphologies of the EFPs formed using the different polygonal charges.

Figure 20 depicts the morphologies of the EFPs formed using the different polygonal charges. The number of fins was equal to the number of polygon sides. As the number of polygon sides increased, the EFP length-to-diameter ratio and compactness values increased, the EFP velocity did not vary substantially, and the tail-to-head diameter ratio decreased; the rates of change of these values decreased as the number of sides increased. Figure 21 presents a graphic representation of the performance measures of the EFPs formed using the different polygonal charges. When the number of polygon sides was excessively large (i.e., the warhead was approximately a circular column), the tail fins resembled a skirt and the velocity gradient increased from the EFP head to the tail, which resulted in an increased length-to-diameter ratio and a higher fracture risk. These results indicate that tail fin EFPs formed using polygonal charges with the same basic structural parameters, but different numbers of sides, had considerably different morphologies. Therefore, polygonal charges with different numbers of sides had substantially different optimal structural parameter values.

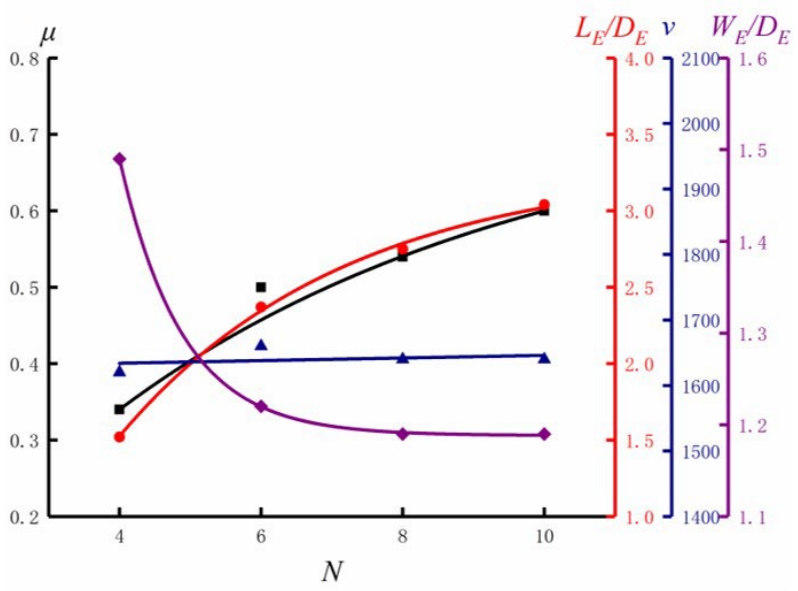

Figure 21 Values of v, L_E/D_E, μ, and W_E/D_E for tail fin EFPs formed using polygonal charges with different numbers of sides.

5 CONCLUSIONS

In this study, a polygonal charge capable of forming tail fin EFPs was designed, and the tail fin EFP formation process, along with its underlying mechanisms, was analyzed by combining a theoretical analysis with numerical simulations and an experiment. The study produced four conclusions:

(1) By incorporating the principles of effective charge theory and detonation ejection theory, along with the application of calculus, a calculation model for the formation speed of EFP has been developed. The theoretical results obtained from this model show good agreement with experimental and simulation data. Furthermore, it is observed that under the polygonal charge structure, the velocity distribution of the liner increases gradually along the circumferential direction as the charge diameter increases.

(2) Under appropriate structural parameter matching, a polygonal charge warhead can indeed form a tail fin EFP, with the number of tails being consistent with the number of edges.

(3) For an EFP warhead formed using a polygonal charge, the compactness, μ, was positively related to the liner radius of curvature, R_1, and the shell thickness, h_{s0}, while it was negatively related to the liner center thickness, h_l, and the charge height, L. The length-to-diameter ratio, L_E/D_E, was positively related to L and negatively related to R_1, h_l, and h_{s0}. The EFP velocity was negatively related to R_1, L, and h_{s0} and negatively related to h_l. W_E/D_E was positively related to h_l and h_{s0} and negatively related to R_1.

(4) The ranges of optimal values for the structural parameters of a hexagonal charge capable of forming high-performance tail fin EFPs were determined: R_1 should be in the $0.75D_c$–$0.85D_c$ range, h_l should be in the $0.0486D_c$–$0.06D_c$ range, L has an optimal value in the $0.75D_c$–$1.05D_c$ range, and h_{s0} should be in the $0.06D_c$–$0.10D_c$ range.

(5) As the number of polygon sides increased, the tail fin EFP length-to-diameter ratio and compactness values increased while velocity did not vary substantially, and the tail fins of EFP gradually turns to the skirt.

Acknowledgments

The work presented in this paper was funded by the China Postdoctoral Science Foundation (Grant No. 2022M721614).

Author's Contributions: Writing - original draft and Writing - review & editing, Peng Chen; Conceptualization, Wenbin Li; Funding acquisition, Yiming Li; Supervision, Dacheng Gao.

Editor: Marcílio Alves

References

Benham R A. Terminal velocity and rotation rate of a flyer plate propelled by a tube-confined explosive charge[J]. 1979.

Berner C and Flec V, “Pleat and asymmetry effects on theaerodynamics of explosively formed penetrators,” in Pro-ceedings of the 18th International Symposium on Ballistics, pp. 11–19, TX institute for Advanced Technology-The University of Texas at Austin Southwest Research Institute, San Antonio, 1999.

Bouet T, Tarayre P, Guillon J P. Study of a multi-point ignition EFP [J]. 1995.

Cao B. Study on detonation of charge and EFP forming phenomenon under multi-point initiation [D].Nanjing:Nanjing University of Science and Technology,1998.

Chuan Y, Yanjin T, Chengli Y, et al. Applied research of shaped charge technology[J]. International Journal of Impact Engineering, 1999, 23(1): 981-988.

Fu H, Jiang JW, Men JB, et al. Microstructure Evolution and Deformation Mechanism of Tantalum–Tungsten Alloy Liner under Ultra-High Strain Rate by Explosive Detonation[J]. Materials, 2022, 15(15): 5252.

Huang J, Zhang QM. Distortion of a Liner Under Sliding Detonation [J]. Transactions of Beijing Institute of Technology,2009,29(04):286-289.

Huang X, Li W, Li W, et al. Energy Spatial Distribution of Behind-Armor Debris Generated by Penetration of Explosively Formed Projectiles with Different Length–Diameter Ratio[J]. Applied Sciences, 2023, 13(4): 2665.

Hussain G, Hameed A, Hetherington J G, et al. Hydrocode simulation with modified Johnson-Cook model and experimental analysis of explosively formed projectiles[J]. Journal of Energetic Materials, 2013, 31(2): 143-155.

Jeremić O, Milinović M, Marković M, et al. Analytical and numerical method of velocity fields for the explosively formed projectiles[J]. FME Transactions, 2017, 45(1): 38-44.

Johnson R, Cook W K. A constitutive model and data for metals subjected to large strains high strain rates and high temperatures. The 7th International Symposium on Ballistics [J]. 1983.

Kennedy J E. The gurney model of explosive output for driving metal[J]. Explosive effects and applications, 1998: 221-257.

Li CB, Shen ZW, Pei MJ. Investigation of Three-point Detonation Mechanism and Formation of Tails of EFP [J]. Chinese Journal of Energetic Materials, 2007, (01): 23-8.

Li R, Li WB, Wang XM, et al. Effects of Three-point Initiation Synchronization Error on Formation Performance of EFP with Fins[J]. Chinese Journal of Energetic Materials, 2016a,24(11):1041-1047.

Li R, Li WB, Wang XM. Effects of control parameters of three-point initiation on the formation of an explosively formed projectile with fins [J]. Shock Waves 2018;28(5): 1–14.

Li W, Wang X, Li W, et al. Research on the skirt tail explosively formed projectile stable shaping technology[J]. Journal of Applied Mechanics and Technical Physics, 2016b, 57: 894-899.

Li WB, Dong XL, Shen XJ, et al. Simulation Study on EFP with Stable Tail Fins Formed by Polygonal Shaped Charge Liner. In: Proceedings of the 31st international symposium on ballistics; 2019. p. 1899–908.

Li YB, Wang JX, Liu ZT, et al. Orthogonal optimization design and experiments on explosively formed projectiles with fins[J]. International Journal of Impact Engineering, 2023,173:104462.

Li YC, Yang WJ, Shen W. Influence of Liner Curvature Radius on Parameters of Explosively Formed Penetrator (EFP) [J]. Explosive device, 2003 (1): 4.

Liu J, Chen X, Du Z. A study on the surface overpressure distribution and formation of a double curvature liner under a two-point initiation[J]. Defence Technology,2022,18(01):148-157.

Liu JF, Yuan L, Chong J, et al. Dynamic Response and Microstructure Evolution of Oxygen-Free High-Conductivity Copper Liner in Explosively Formed Projectile [J]. Latin American journal of solids and structures, 2017, 14(11): 2089-106.

Liu JQ, Gu WB, Lu M, et al. Formation of explosively formed penetrator with fins and its flight characteristics [J]. Defence Technology, 2014a, (2): 5.

Liu JQ, Gu WB, Xu HM, et al. Effects of multi-point initiation charge configuration parameters on EFP with fins formation [J]. Chinese Journal of Energetic Materials, 2014b;22(5):594–9.

Lin JJ, Shen ZW, Ren HQ, et al. Experimental Study on Explosively Formed Projectiles with Fins and Numerical Simulation [J]. Chinese Journal of Explosives &Propellants, 2009, 32(1): 5.

Lin JJ, Shen ZW, Ren HQ, et al. Mechanism Discussion on Explosively Formed Projectile with Fins by Affixing Partition [J]. BLASTING, 2013, 30(2): 8.

Luo ZW, Tang Y, Gu WB, et al. Numerical Simulation study of performance of Empennage forming of liner with five concaver arc margins cutted[J]. Blasting 2009; 26(1):29–33.

Ma HB, Zheng YF, Wang HF, et al. Formation and impact-induced separation of tandem EFPs [J]. Defence Technology, 2020;16(3):668–77.

Men JB, Jiang JW, Wan LZ. 3D Numerical Simulation Research on the Formation of Explosively Formed Penetrator with Fins[J]. Transactions of Beijing institute of Technology, 2002, (2): 166-168.

Orilenko, Л. П. 2011. Explosion physics, S. U. N. Chengwei. Translated by. Beijing: Science Press. in Chinese.

Peng J, Jiang J, Men J, et al. Explosively Formed Projectile from Stepped Casing Shaped Charge: Formation Mechanism of Canted Fins[J]. Journal of Energetic Materials, 2022: 1-22.

Sharma V K, Kishore P, Bhattacharyya A R, et al. An analytical approach for modeling efp formation and estimation of confinement on velocity[J]. International ballistic society, 2001: 565-574.

Shi DY, Zhang QM, Xia CF, et al. Numerical simulation of explosively formed projectile with canted fins by asymmetrical casing[J]. Initiators & Pyrotechnics, 2010;(4):17–20.

Tang PJ, Gu WB, Lu ZW. Effect of variable wall thickness shell on the formation of EFP with tail[J]. Journal of Ordnance Equipment Engineering, 2009;30(1):34–6. +57.

Wang RC, Zhao GZ. Terminal effects of projectile[M]. Beijing: Beijing Institute of Technology Press,1993:100-101.

Wang SY, Jiang JW, Men Jianbin. Numerical simulation of parameters on formation of quasi-spherical EFP[J]. Chinese Journal of Energetic Materials, 2011, 16(6): 731-733.

Wang W, Chen Z, Yang B, et al. Formation of an Explosively Formed Penetrator Warhead Using a Step-Shaped Charge[J]. Shock and Vibration, 2022, 2022.

Wang YY, Jiang JW, Meng JY, et al. Effect of add-on explosive reactive armor on EFP penetration[C]//29th International Symposium on Ballistics. 2016.

Weimann K. Arrangement for production of explosively formed projectiles: U.S. Patent 4,982,667[P]. 1991-1-8.

Weimann K. Research and development in the area of explosively formed projectiles charge technology [J]. Propellants, explosives, pyrotechnics, 1993;18(5):294–8.

Wu J, Liu J, Du Y. Experimental and numerical study on the flight and penetration properties of explosively-formed projectile[J]. International journal of impact engineering, 2007, 34(7): 1147-1162.

Yu JS, Liu TS, Shi JL, et al. Numerical analysis of the effect of polygonal shell on the forming process of explosively formed projective with tail fins[J]. Initiators & Pyrotechnics, 2017(06):19-22.

Yang D, Lin J. Numerical investigation on the formation and penetration behavior of explosively formed projectile (EFP) with variable thickness liner[J]. Symmetry, 2021, 13(8): 1342.

Zhang PX, Shen XJ, You N, et al. A new method for generation of finned EFP [J]. Journal of Projectiles, Rockets, Missiles and Guidance,2004;24(1):147–9.

Zhao HY, Shen ZW, Li CB, et al. A New Way of Explosively Formed Projectile with Stabilizing Fins [J]. Chinese Journal of Energetic Materials,2006(02):102-104.

Zhu CS. Research on forming technology of explosively formed projectile warhead with partition[D]. Nanjing University of Science and Technology, 2014.